



Wei-Jung Yen,<sup>a</sup> Jian-Hong Liao,<sup>a</sup> Tzu-Hao Chiu,<sup>a</sup> Jie-Ying Chen,<sup>b</sup> Yuan Jang Chen,<sup>b</sup> Samia Kahlal,<sup>c</sup> Jean-Yves Saillard <sup>\*c</sup> and C. W. Liu <sup>\*a</sup>

[rsc.li/nanoscale](http://rsc.li/nanoscale)

This study investigates the effects of metal addition and doping of a 2-electron silver superatom,  $[\text{Ag}_{10}(\text{S}_2\text{P}(\text{O}^i\text{Pr})_2)_8]$  (**Ag<sub>10</sub>**). When  $\text{Ag}^+$  is added to **Ag<sub>10</sub>** in THF solution,  $[\text{Ag}_{11}(\text{S}_2\text{P}(\text{O}^i\text{Pr})_2)_8(\text{OTf})]$  (**Ag<sub>11</sub>**) is rapidly formed almost quantitatively. When the same method is used with  $\text{Cu}^+$ , a mixture of alloys,  $[\text{Cu}_x\text{Ag}_{11-x}(\text{S}_2\text{P}(\text{O}^i\text{Pr})_2)_8]^+$  ( $x = 1-3$ , **Cu<sub>x</sub>Ag<sub>11-x</sub>**), is obtained. In contrast, introducing  $\text{Au}^+$  to **Ag<sub>10</sub>** leads to decomposition. The structural and compositional analysis of **Ag<sub>11</sub>** was characterized by single-crystal X-ray diffraction (SCXRD), ESI-MS, NMR spectroscopy, and DFT calculations. While no crystal structure was obtained for **Cu<sub>x</sub>Ag<sub>11-x</sub>**, DFT calculations provide insights into potential sites for copper location. The absorption spectrum exhibits a notable blue shift in the low-energy band after copper doping, contrasting with that of the slight shift observed in 8-electron Cu-doped Ag nanoclusters. **Ag<sub>11</sub>** and **Cu<sub>x</sub>Ag<sub>11-x</sub>** are strongly emissive at room temperature, and solvatochromism across different organic solvents is highlighted. This study underscores the profound influence of metal addition and doping on the structural and optical properties of silver nanoclusters, providing important contributions to understanding the nanoclusters and their photophysical behaviors.

Noble metal nanoclusters (NCs), predominantly composed of gold, silver, and copper, represent a novel and promising class of functional materials exhibiting numerous unique characteristics.<sup>1–19</sup> These atomically precise NCs stand apart from nanoparticles, showcasing significant differences in various properties including electronic and absorption properties,<sup>1,2,5–8</sup> photoluminescence,<sup>1,2,6–9</sup> magnetism,<sup>10,11</sup> catalytic activity,<sup>12–14</sup> and biomedical applications.<sup>15,16</sup> Recent studies have established that the intrinsic properties of a homometallic NC can be altered through the incorporation of heterometals, leading to improved properties.<sup>1,2,6,8,17–22</sup> Contemporary research is now largely devoted to designing and tailoring the properties of NCs to suit particular applications in a predictable and manageable manner. Specifically, the stability and catalytic activity of Au NCs can be significantly

enhanced by doping with Pt, Pd, Ag, Cu, or other foreign metal atoms.<sup>23–26</sup> Furthermore, Au/Ag bimetallic NCs have been observed to display greater photoluminescence quantum yield (PLQY) when compared to homometallic Ag NCs.<sup>22,27</sup> It is important to note that the field of NC chemistry still holds a plethora of uncharted potential properties that is yet to be explored and understood.

Copper, as well as the other group 11 metals, possesses multiple coordination versatility and has attracted significant interest due to its outstanding efficacy in CO<sub>2</sub> reduction.<sup>28,29</sup> However, when incorporated as a dopant into NCs, Cu exhibits distinct influences on the structure and characteristics of the NCs, in contrast to the effects observed with Au or Ag atoms. In the case of Cu alloying, the Cu atoms tend to position themselves in the shell layer of the core-shell NCs.<sup>30–35</sup> Zhu *et al.* reported bimetallic NCs, Au<sub>36–x</sub>Cu<sub>x</sub>(*m*-MBT)<sub>24</sub> (*x* = 1–3),<sup>30</sup> Au<sub>38–x</sub>Cu<sub>x</sub>(2,4-DMBT)<sub>24</sub> (*x* = 0–6, DMBT = 2,4-dimethylbenzenethiolate),<sup>31</sup> and [Ag<sub>62–x</sub>Cu<sub>x</sub>S<sub>12</sub>(SBU)<sub>32</sub>]<sup>4+</sup> (*x* = 10–21).<sup>32</sup> Liu *et al.* reported bimetallic Cu<sub>x</sub>Ag<sub>20–x</sub>{S<sub>2</sub>P(OR)<sub>2</sub>}<sub>12</sub> (*x* = 3, 4; R = <sup>i</sup>Pr,<sup>19</sup> <sup>n</sup>Pr<sup>33</sup>). These studies consistently demonstrated a marked tendency for Cu atoms to favor surface positions, displaying disordered arrangements across multiple sites instead of situating themselves within the core. This behavior can be attributed to the lower reduction potential of Cu<sup>+</sup> (0.52 and 0.80 V for Cu<sup>I</sup>/Cu<sup>0</sup> and Ag<sup>I</sup>/Ag<sup>0</sup>, respectively, *vs.* SHE, *T* = 25 °C, 1 atm), which hampers the anti-galvanic reaction (AGR) with the kernel Ag/Au atoms, making it challenging to proceed.<sup>36</sup> Consequently, a metal exchange occurring at the surface

† Electronic supplementary information (ESI) available: NMR spectrum, TD-DFT spectrum, XPS, photophysical data. CCDC 2287343. For ESI and crystallographic data in CIF or other electronic format see DOI: <https://doi.org/10.1039/d4nr00326h>

M(i) atoms emerges as a more favorable process. To the best of our knowledge, the chemistry of 2-electron Ag/Cu superatomic alloys has never been explored. Kappes *et al.* reacted the 8-electron cluster  $[\text{Ag}_{29}(\text{BDT})_{12}(\text{PPh}_3)_4]^{3-}$  (BDT = 1,3 benzenedithiolate) with  $\text{Cu}_{12}\text{S}_6(\text{DPPPT})_4$  (DPPPT = bis-(diphenylphosphino) pentane), yielding the alloys  $[\text{Ag}_{29-x}\text{Cu}_x(\text{BDT})_{12}]^{3-}$  ( $x = 0-13$ ).<sup>37</sup> Although they could not obtain any crystal structures, they performed DFT calculations to determine the Cu locations in the alloy shells and found a preference for the outermost positions. Conversely, in the case of the 46-electron  $[\text{Cu}_{30}\text{Ag}_{61}(\text{SAdm})_{38}\text{S}_3]^+$ , the Cu atoms are found to be located within the interior of the NCs.<sup>38</sup> This compound presents an onion-type structure, conceptualized as  $[\text{Ag}_{13}@\text{Cu}_{30}@\text{Ag}_{48}(\text{SAdm})_{38}\text{S}_3]^+$ . Here, the Cu atoms are situated in the second inner shell, sandwiched between the  $\text{Ag}_{13}$  icosahedral core and the outermost  $\text{Ag}_{48}(\text{SAdm})_{38}\text{S}_3$  shell. This distinct arrangement highlights the unique distribution of Cu atoms participating in the NC's architecture.

Following our previous research on the doping effect on 8-electron superatoms,<sup>16,33</sup> we chose the 2-electron Ag NC  $[\text{Ag}_{10}(\text{dtp})_8]$  ( $\text{dtp} = \text{S}_2\text{P}(\text{O}^i\text{Pr})_2$ ) (**Ag<sub>10</sub>** for short)<sup>39</sup> as the starting template. The subsequent addition of Ag(i) and Cu(i) ions yield  $[\text{Ag}_{11}(\text{dtp})_8(\text{SO}_3\text{CF}_3)]$  (**Ag<sub>11</sub>** for short) and  $[\text{Cu}_x\text{Ag}_{11-x}(\text{dtp})_8]^+$  ( $x = 0-3$ ) (**Cu<sub>x</sub>Ag<sub>11-x</sub>** for short), respectively.

## Results and discussion

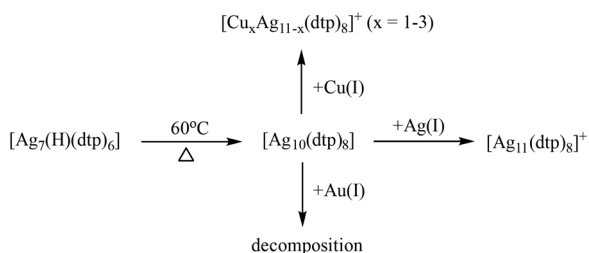
In the course of the synthesis (Scheme 1),  $\text{Ag}(\text{OTf})$  was introduced into a THF solution of **Ag<sub>10</sub>** with a 1 : 1 molar ratio at ambient temperature. The reaction could be concluded within only one minute, resulting in the production of **Ag<sub>11</sub>** with an impressive yield of up to 97%. This success attests to the viability of adding extra Ag(i) ions to Ag NCs, a strategy corroborated by previous research involving the transformation of  $[\text{Ag}_7(\text{H})\text{L}_6]$  into  $[\text{Ag}_8(\text{H})\text{L}_6]^+$  ( $\text{L} = \text{dithiophosphate}$  or  $\text{diselenophosphate}$ )<sup>40</sup> and  $[\text{Ag}_{20}\{\text{S}_2\text{P}(\text{O}^i\text{Pr})_2\}_{12}]$  into  $[\text{Ag}_{21}\{\text{S}_2\text{P}(\text{O}^i\text{Pr})_2\}_{12}]^+$ .<sup>41</sup> Following the same reaction conditions as those for **Ag<sub>11</sub>**, the introduction of one equivalent of  $[\text{Cu}(\text{CH}_3\text{CN})_4](\text{OTf})$  facilitated the formation of **Cu<sub>x</sub>Ag<sub>11-x</sub>**. In contrast, the addition of  $\text{Au}(\text{PPh}_3)\text{Cl}$  into **Ag<sub>10</sub>** led to decomposition. Notably, Au-doped NCs, such as  $[\text{Au}_1\text{Ag}_{22}(\text{SAdm})_{12}]^{3+}$  (8e),<sup>42</sup>  $\text{Au}_x\text{Ag}_{50-x}(\text{Dppm})_6(\text{SR})_{30}$  (20e),<sup>43</sup> and  $[\text{Ag}_{46}\text{Au}_{24}(\text{SR})_{32}]^{2+}$  (36e),<sup>44</sup> exhibit enhanced thermal stability. Au atoms on the surface typically form an S-Au-S linear

coordination with ligands.<sup>45</sup> When the gold atom is located in the kernel, Au is singly bonded to the S atom,<sup>46</sup> constraining the doping positions available. The challenge becomes pronounced in the **Ag<sub>10</sub>** structure, where each Ag atom is bonded to two or three sulfur atoms. Au doping may alter the original coordination environment, resulting in an inability to maintain the structural framework.

The positive-ion ESI-MS of **Ag<sub>11</sub>** (Fig. 1) reveals a molecular ion peak at  $m/z$  2892.2122 Da, aligning with its cationic counterpart  $[\text{Ag}_{11}(\text{dtp})_8]^+$  (calc. 2892.0923 Da). The experimental isotopic distribution showcases a good agreement with the simulated pattern. A fragmentation peak at 2250.5063 Da was observed, which corresponds to  $[\text{Ag}_9(\text{dtp})_6]^+$  (calc. 2250.2461 Da). A peak at 2178.5623 Da can be assigned to  $[\text{Ag}_8(\text{Cl})(\text{dtp})_6]^+$  (calc. 2178.3088 Da). It is postulated that such species could be formed during sample preparation in  $\text{CH}_2\text{Cl}_2$  solution, prior to the mass spectrometry measurement. The ESI-MS of **Cu<sub>x</sub>Ag<sub>11-x</sub>** (Fig. 2a) reveals a distribution of  $[\text{Cu}_x\text{Ag}_{11-x}(\text{dtp})_8]^+$  ( $x = 0-3$ ) with the **Cu<sub>1</sub>Ag<sub>10</sub>** ( $x = 1$ ) species assigned to the most intense band. Such a distribution was also observed in other Cu-doped Ag NCs, such as  $[\text{Cu}_x\text{Ag}_{20-x}(\text{dtp})_{12}]$  ( $\text{R} = ^i\text{Pr}$ ,  $x = 1-7$ ;  $\text{R} = ^n\text{Pr}$ ,  $x = 0-5$ ),<sup>19,33</sup>  $[\text{Ag}_{29-x}\text{Cu}_x(\text{BDT})_{12}]^{3-}$  ( $x = 0-13$ ),<sup>37</sup> and  $[\text{Ag}_{62-x}\text{Cu}_x\text{S}_{12}(\text{SBU})_{32}]^+$  ( $x = 10-21$ ).<sup>32</sup>

The  $^{31}\text{P}\{^1\text{H}\}$  NMR spectrum of **Ag<sub>11</sub>** (Fig. S2†) shows two chemical shifts at 100.8 and 103.2 ppm, with an integration ratio of approximately 6 : 2, which corresponds to the two coordination environments of the dtp ligands. These resonances are shifted to 104.5 and 105.4 ppm in **Ag<sub>10</sub>**. The  $^{31}\text{P}\{^1\text{H}\}$  NMR spectrum (Fig. S4†) of **Cu<sub>x</sub>Ag<sub>11-x</sub>** shows multiple resonances spanning a broad range from 94 to 105 ppm, suggesting that the copper substitution within the **Ag<sub>11</sub>** framework may occur at various positions, leading to a diversity of chemical environments.

In the molecular architecture of **Ag<sub>10</sub>**, a conspicuous vacant site can be identified within the shell (Fig. 3a), presenting itself as an ideal location for hosting an additional metal anion and creating locally an  $\text{MS}_3$  motif. The additional



**Scheme 1** The route of heterometal doping of **Ag<sub>11</sub>**.

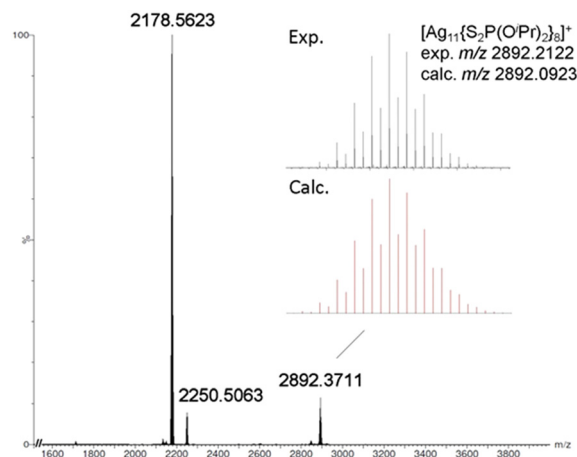


**Fig. 1** The positive-ion ESI-MS of **Ag<sub>11</sub>**.

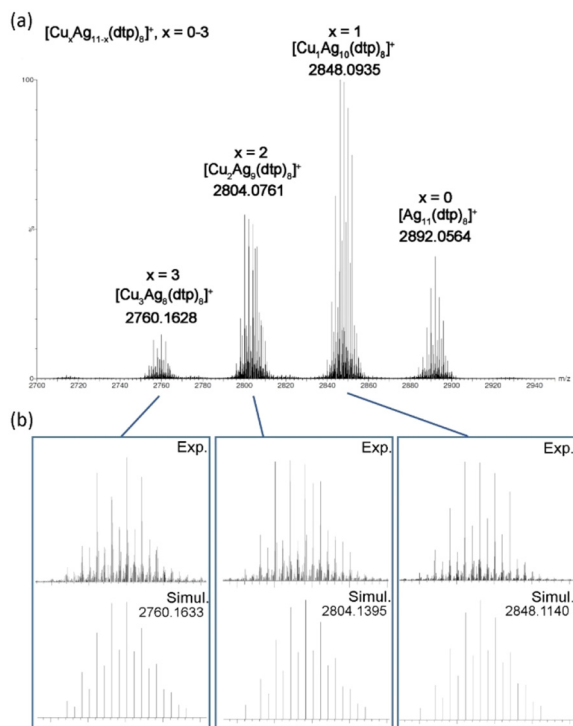


Fig. 2 (a) The positive-ion ESI-MS of  $\text{Cu}_x\text{Ag}_{11-x}$ . (b) The experimental and simulated isotopic distribution patterns of  $\text{Cu}_x\text{Ag}_{11-x}$  ( $x = 1-3$ ).

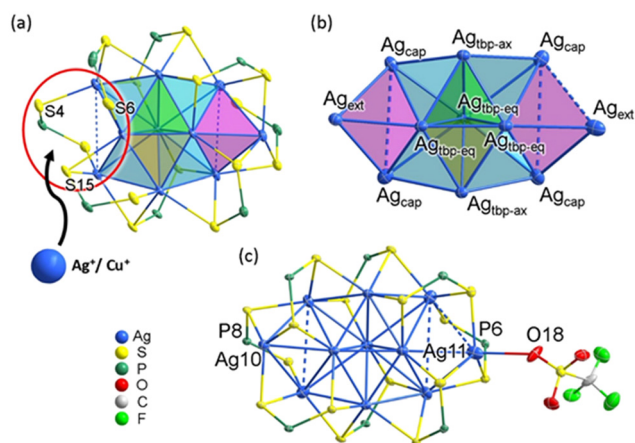


Fig. 3 (a) The structure of  $\text{Ag}_{10}$ . (b) The metal skeleton in  $\text{Ag}_{11}$ . (c) The total structure of  $\text{Ag}_{11}$ . The isopropoxy groups were omitted for clarity.

$\text{Ag}^+$  ion is indeed attached to this precise location, in the crystal structure of  $\text{Ag}_{11}$ . The metal skeleton in  $\text{Ag}_{11}$  is composed of a trigonal bipyramid with four capping ( $\text{Ag}_{\text{cap}}$ ) and two external ( $\text{Ag}_{\text{ext}}$ ) atoms (Fig. 3b). With the addition of an extra silver atom, the metal framework attains higher symmetry, transitioning from  $C_1$  in  $\text{Ag}_{10}$  to  $C_{2v}$  in  $\text{Ag}_{11}$ . The average  $\text{Ag}\cdots\text{Ag}$  distances within the yellow (2.8339(7) Å), green (2.8386(7) Å), and cyan (2.9778(7) Å) tetrahedra in  $\text{Ag}_{11}$  are similar to those in  $\text{Ag}_{10}$  (yellow: 2.8562(13) Å; green: 2.8553(13) Å, and cyan: 2.9495(13) Å). However, in  $\text{Ag}_{11}$ , the two magenta tetra-

dra exhibit substantially elongated  $\text{Ag}\cdots\text{Ag}$  distances, averaged at 3.2191(8) Å and 3.3555(9) Å, which are notably longer than the 3.150(1) Å observed in  $\text{Ag}_{10}$ . A weak interaction between the OTf anion and the Ag11 atom ( $\text{O18-Ag11}$ : 2.61(1) Å) results in a significant elongation between  $\text{Ag}_{\text{ext}}$  and the triangular base it caps ( $\text{Ag11} - \Delta$ : 2.619 Å,  $\text{Ag10} - \Delta$ : 2.375 Å, see Fig. 3c). These bond lengths are summarized in Table S1.† The coordination modes of the eight dtp ligands in  $\text{Ag}_{11}$  vary: P6 and P8 exhibit an  $\eta^3$  ( $\mu_1, \mu_2$ ) coordination pattern, while the other six ligands demonstrate  $\eta^4$  ( $\mu_2, \mu_2$ ) pattern. This differentiation is reflected in the ambient-temperature  $^{31}\text{P}\{^1\text{H}\}$  NMR spectrum, where two chemical shifts are observed. Consequently, these coordination differences contribute to the overall  $[\text{Ag}_{11}(\text{dtp})_8]^+$  molecule possessing approximate  $C_2$  symmetry.

Despite our inability to determine the crystal structures of  $\text{Cu}_x\text{Ag}_{11-x}$  directly, ESI-MS data indicate that the species with the highest intensity is  $\text{Cu}_1\text{Ag}_{10}$ . This observation leads us to hypothesize that the doping copper atom predominantly occupies the NC's outermost fringe (*i.e.*  $\text{Ag}_{\text{ext}}$ , see Fig. 3a), and the geometry of  $\text{Cu}_1\text{Ag}_{10}$  closely resembles the core skeleton of  $[\text{Cu}_x\text{Ag}_{10-x}(\text{Se})(\text{dsep})_8]$  ( $x = 3-4$ ,  $\text{dsep} = \text{Se}_2\text{P}(\text{O}^i\text{Pr})_2$ , see Fig. S6†).<sup>47</sup> Moreover, in scenarios where additional copper substitution would occur, it is likely that these copper atoms would prefer being situated at the other  $\text{Ag}_{\text{ext}}$  or  $\text{Ag}_{\text{cap}}$  positions (Fig. S7†). To substantiate this hypothesis, we employed DFT calculations, wherein 1, 2 and 3 Cu atoms were systematically substituted in the original  $\text{Ag}_{11}$  structure (*vide infra*).

The absorption spectrum of  $\text{Ag}_{11}$  exhibits two prominent bands at 390 and 528 nm (Fig. 4a). The high-energy band at approximately 366 nm is barely seen, embedded in the shoulder. This pattern shows similarity to that of the previously reported  $\text{Ag}_{10}$ , which exhibits bands at 348, 392, and 520 nm.<sup>39</sup> In the case of the copper-doped  $\text{Cu}_x\text{Ag}_{11-x}$  NC, a noticeable blue shift of the low-energy band, moving to 506 nm, while the high-energy band at 392 nm remains relatively unchanged. This behavior contrasts with that of the previously investigated 8-electron NCs,<sup>19,33</sup> where Cu doping did not markedly alter the three primary absorption bands. Notably, the low-energy band around 480 nm remains consistent between the  $[\text{Cu}_4\text{Ag}_{17}(\text{dtp})_{12}]^+$  and  $[\text{Ag}_{21}(\text{dtp})_{12}]^+$  structures.<sup>19</sup> This could be attributed to the larger core structure of the NC, which likely positions the surface-integrated copper atoms at a greater distance from the core, thereby minimizing their influence on the absorption characteristics.

The time-dependent-DFT (TD-DFT) simulated UV-vis spectra of  $\text{Ag}_{11}$  and of the most stable isomer of  $\text{Cu}_x\text{Ag}_{11-x}$  ( $x = 1-3$ ) (see the Computational details section) are shown in Fig. S8.† They exhibit the same shape as their experimental counterparts (*vide supra*). For all the compounds, the band of lowest energy can be identified as the HOMO ( $1\text{S}$ )  $\rightarrow$  LUMO ( $1\text{P}_x$ ) transition, whereas the high-energy band is of mixed HOMO ( $1\text{S}$ )  $\rightarrow$  LUMO+1 ( $1\text{P}_z$ ) and ligand  $\rightarrow$  LUMO ( $1\text{P}_x$ ) character (see the  $1\text{S}^2 1\text{P}^0$  electronic structure DFT analysis), with little Cu participation in these two bands in the case of the  $\text{Cu}_x\text{Ag}_{11-x}$  alloys. In the case of  $\text{Ag}_{11}$ , the two simulated peaks appear at 559 and 384 nm, values which compare relatively

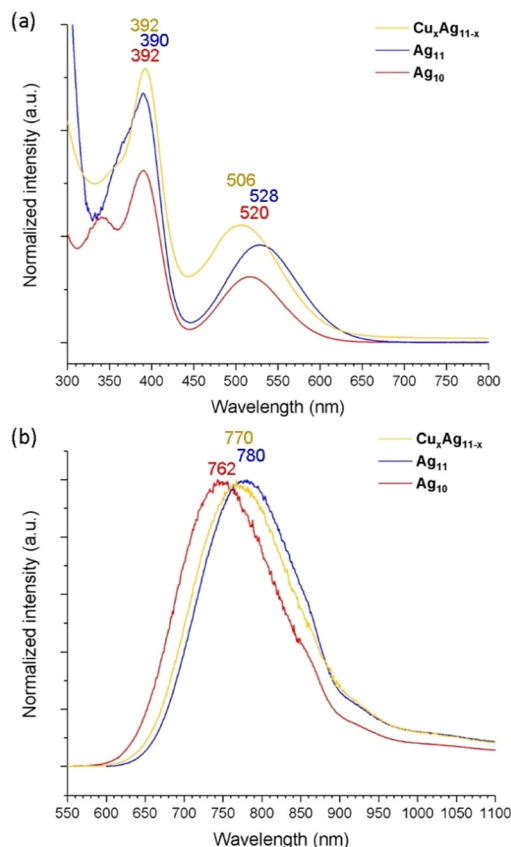


Fig. 4 (a) The ambient-temperature UV-vis absorption spectra and (b) emission spectra of  $\text{Ag}_{10}$ ,  $\text{Ag}_{11}$  and  $\text{Cu}_x\text{Ag}_{11-x}$ .

well with their experimental counterparts, 528 and 390 nm, respectively. In the case of the  $\text{Cu}_x\text{Ag}_{11-x}$  alloys, the high-energy band is barely perturbed, while the low-energy band is more blue-shifted as the number of copper atoms increases. This trend matches well with the experimental spectra (*vide supra*). The blue shift of the low-energy band is related to the increase of the  $1\text{S} \rightarrow 1\text{P}_x$  gap (mainly a LUMO destabilization) with the increase in the number of Cu atoms in the NC. On the other hand, the  $1\text{S} \rightarrow 1\text{P}_z$  transition participates to a lesser extent in the high-energy band and, having less Cu character, it is also less sensitive to the Cu content, explaining the inertness of this band to Cu alloying.

The room-temperature emission spectrum (Fig. 4b) exhibits a red shift in peak wavelength from 762 nm for  $\text{Ag}_{10}$  to 780 nm for  $\text{Ag}_{11}$ , marking a transition to the near-infrared (NIR) region upon metal addition, while copper doping to form  $\text{Cu}_x\text{Ag}_{11-x}$  results in the emission maxima shifting from 762 nm to 770 nm, a slight blue shift compared with  $\text{Ag}_{11}$ , which correlates well to the observed blue shift in the low-energy absorption band. This movement toward NIR emission in these NCs is advantageous for bioimaging applications due to deeper tissue penetration capabilities and minimized photodamage.<sup>15,16,48</sup> On the other hand,  $\text{Ag}_{11}$  exhibits an enhanced QY of 14.6%, a significant increase from the 6.0% observed in  $\text{Ag}_{10}$ . The enhancement can be caused by the

increased nuclearity in  $\text{Ag}_{11}$ , which effectively stabilizes the surface ligand, thereby reinforcing its rigidity in solution. However, the QY decreases to 7.8% in  $\text{Cu}_x\text{Ag}_{11-x}$  compared to  $\text{Ag}_{11}$ . This reduction may be due to intercluster reactions occurring within the solution, where copper atoms are exchanged between NCs. This phenomenon is akin to the observed intercluster reactions in  $\text{Ag}_7(\text{H})(\text{dtp})_6$  and  $\text{Cu}_7(\text{H})(\text{dtp})_6$ , leading to a similar exchange of copper atoms.<sup>49</sup> Furthermore, the PLQY experiences a notable enhancement in the film state, reaching 37.2% for  $\text{Ag}_{11}$  and 16.1% for  $\text{Cu}_x\text{Ag}_{11-x}$  (Table S3†). The lifetimes of  $\text{Ag}_{11}$  and  $\text{Cu}_x\text{Ag}_{11-x}$  are in the nanosecond range, with 5.37 and 6.33 ns at RT (Fig. S11 and S13†), and 15.43 and 13.69 ns at 77K (Fig. S12 and S14†). The photophysical data are summarized in Table 1. Overall, the result suggests the resilience of superatomic electronic properties, which demonstrates the fine-tuning property following its metal addition or the Cu doping in the ultrasmall NCs.

Structural insights reveal that in  $\text{Ag}_{11}$ , the OTf anion exhibits a weak interaction with the  $\text{Ag}_{\text{ext}}$  site, and the  $\text{Ag}_{\text{ext}}\text{S}_3$  motif is nearly coplanar, suggesting that  $\text{Ag}_{\text{ext}}$  could readily interact with solvent molecules. The solvatochromic behavior of  $\text{Ag}_{10}$ ,  $\text{Ag}_{11}$ , and  $\text{Cu}_x\text{Ag}_{11-x}$  shows a more pronounced shift upon solvent polarity for  $\text{Ag}_{11}$  (76 meV) and  $\text{Cu}_x\text{Ag}_{11-x}$  (71 meV) compared to  $\text{Ag}_{10}$  (54 meV) (Fig. 5). The emission shifts from negative to positive solvatochromism with increasing solvent polarity. The polarity of solvents is quantified using the polarity parameter ( $E_T$ ), which is defined by the molar transition energy (measured in  $\text{kcal mol}^{-1}$ ).<sup>50</sup> This heightened sensitivity in  $\text{Ag}_{11}$ , and  $\text{Cu}_x\text{Ag}_{11-x}$  may be attributed to their structural configuration, which features a higher number of accessible  $\text{Ag}_{\text{ext}}/\text{Cu}_{\text{ext}}$  sites. These sites are proximal to the superatomic core, where the emission is primarily due to the  $1\text{P}_x \rightarrow 1\text{S}$  transition. Thus, solvent molecules have a significant impact on these NCs by affecting the proximity of  $\text{Ag}_{\text{ext}}/\text{Cu}_{\text{ext}}$  sites to the superatomic core, leading to the observed substantial solvatochromic effect in  $\text{Ag}_{11}$ , and  $\text{Cu}_x\text{Ag}_{11-x}$ .

DFT calculations (see the Computational details section) were first performed on the homometallic  $\text{Ag}_{11}$  cluster, whose optimized geometry (Table 2) is in good agreement with its SCXRD structure (Table S1†). Whereas the metal framework in this optimized geometry approaches  $C_{2v}$  symmetry, that of the whole NC (ligand considered) is very close to  $C_2$ , with the pseudo- $C_2$  axis collinear with the  $(\text{Ag}_{\text{tbp-aq}})_3$  diagonal that is perpendicular to the plane of Fig. 3b. Accordingly, there are two (slightly) different couples of  $\text{Ag}_{\text{cap}}$  atoms, namely  $\text{Ag}_{\text{cap}}^a$  and  $\text{Ag}_{\text{cap}}^b$ .

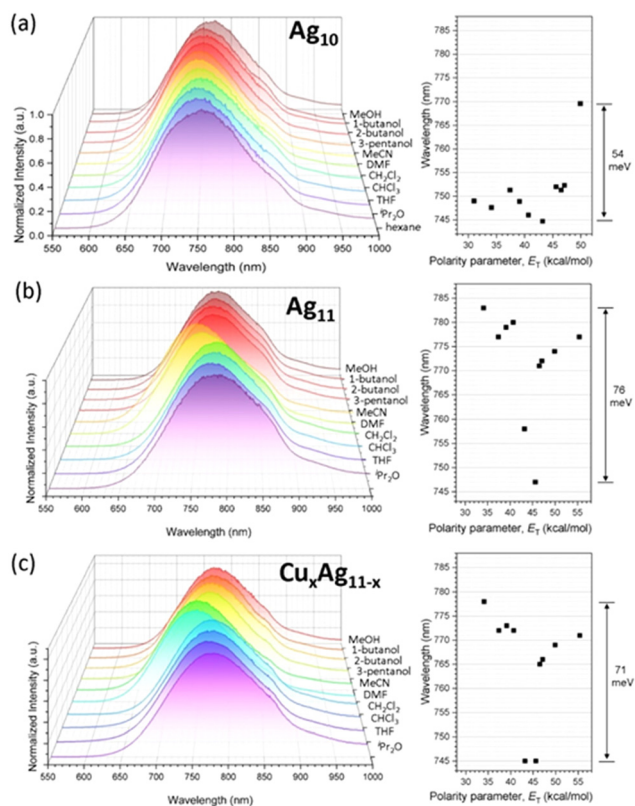
The electronic structure of  $\text{Ag}_{11}$  is strongly related to that of its  $\text{Ag}_{10}$  precursor. Its Kohn–Sham orbital diagram is shown in Fig. 6. The HOMO can be identified as the  $1\text{S}$  superatomic orbital, with some ligand admixture. Its principal metal contribution is from the central trigonal bipyramid, with major participation of the equatorial triangle  $(\text{Ag}_{\text{tbp-eq}})_3$ . Both NAO atomic charges and Wiberg bond indices (Table 2) indicate clearly that the  $\text{Ag}_{\text{cap}}$  and  $\text{Ag}_{\text{ext}}$  atoms do not share any significant part of the two superatomic electrons and can be con-



**Table 1** The photophysical data of  $\text{Ag}_{10}$ ,  $\text{Ag}_{11}$ , and  $\text{Cu}_x\text{Ag}_{11-x}$ 

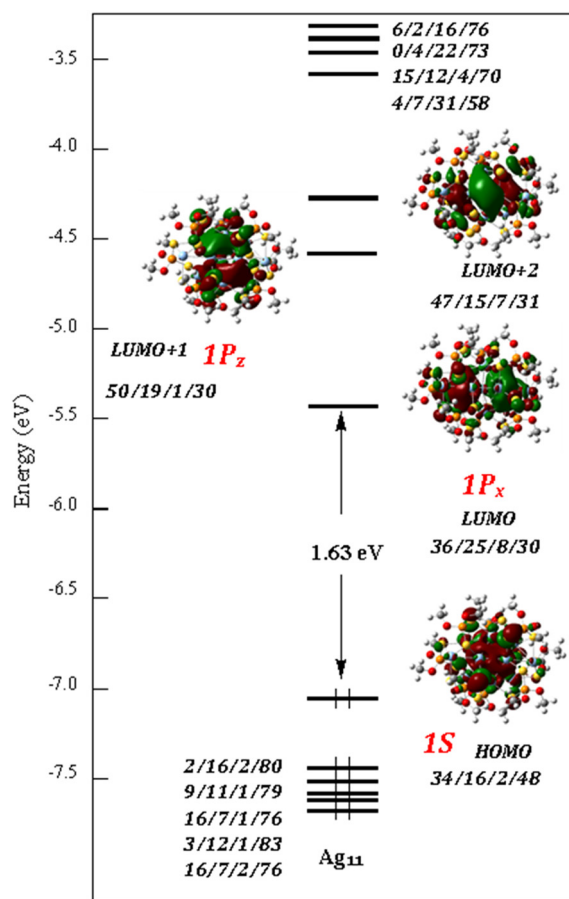
Comp.	State	Absorbance $\lambda_{\text{abs}}$ (nm), $\epsilon$ ( $\text{M}^{-1} \text{cm}^{-1}$ )	Excitation $\lambda_{\text{ex}}$ (nm)	Emission $\lambda_{\text{em}}$ (nm)	Lifetime $\tau$ (ns)	Quantum yield, $\Phi_a$ (%)	$k_r^a$ ( $\text{s}^{-1}$ )	$k_{\text{nr}}^b$ ( $\text{s}^{-1}$ )
$\text{Ag}_{10}$	2-MeTHF, 298 K	348 (15 500), 392 (21 300), 520 (8100)	338, 395, 517	762	1.95	6.0	$3.08 \times 10^7$	$4.82 \times 10^8$
	2-MeTHF, 77 K		335, 388, 515	687	15.37			
$\text{Ag}_{11}$	2-MeTHF, 298 K	390 (20 600), 528 (9000)	391, 530	780	5.37	14.6	$2.72 \times 10^7$	$1.84 \times 10^8$
	2-MeTHF, 77 K		396, 509	699	15.43			
$\text{Cu}_x\text{Ag}_{11-x}$	2-MeTHF, 298 K	392(20 100), 506(8800)	391, 527	770	6.33	7.8	$1.23 \times 10^7$	$1.46 \times 10^8$
	2-MeTHF, 77 K		393, 507	687	13.69			

<sup>a</sup> Radiative rate constant,  $k_r = \Phi_a \times (1/\tau)$ . <sup>b</sup> Nonradiative rate constant,  $k_{\text{nr}} = (1/\tau) - k_r$ .

**Fig. 5** (a) Solvent-dependent emission spectra of  $\text{Ag}_{10}$ , (b)  $\text{Ag}_{11}$ , and (c)  $\text{Cu}_x\text{Ag}_{11-x}$  at RT.**Table 2** Relevant averaged data computed for  $\text{Ag}_{11}$ . WBI = Wiberg bond index

	Distance ( $\text{\AA}$ )	WBI	NAO charges
$\text{Ag}_{\text{tbp-eq}}-\text{Ag}_{\text{tbp-eq}}$	2.868	0.185	$\text{Ag}_{\text{tbp-eq}}$ 0.27
$\text{Ag}_{\text{tbp-ax}}-\text{Ag}_{\text{tbp-eq}}$	2.923	0.093	$\text{Ag}_{\text{tbp-ax}}$ 0.61
$\text{Ag}_{\text{cap}}^{\text{a,b}}-\text{Ag}_{\text{tbp-ax}}$	2.951	0.050	$\text{Ag}_{\text{cap}}^{\text{a}}$ 0.69
$\text{Ag}_{\text{cap}}^{\text{b}}-\text{Ag}_{\text{tbp-eq}}$	3.006	0.063	$\text{Ag}_{\text{cap}}^{\text{b}}$ 0.68
$\text{Ag}_{\text{ext}}-\text{Ag}_{\text{cap}}^{\text{a,b}}$	3.175	0.028	$\text{Ag}_{\text{ext}}$ 0.75
$\text{Ag}_{\text{ext}}-\text{Ag}_{\text{tbp-eq}}$	2.867	0.045	

considered as being in their  $+1$  oxidation state. The two LUMOs can be identified as the superatomic  $1P_x$  and  $1P_z$  orbitals, with some ligand admixture.

**Fig. 6** The Kohn-Sham orbital diagram of  $\text{Ag}_{11}$ . The orbital contribution (in %) is given in the order:  $(\text{Ag}_{\text{tbp}})_5/(\text{Ag}_{\text{cap}}^{\text{a,b}})_4/(\text{Ag}_{\text{ext}})_2/(\text{dtp})_8$ .

In the second step, we investigated the preferred sites of substitution of Ag by Cu in  $\text{Ag}_{11}$ . The main results are summarized in Fig. 7. Based on the computed relative free energies at 298 K, the doping by one Cu atom is almost equally preferred on the  $\text{M}_{\text{ext}}$  and  $\text{M}_{\text{cap}}^{\text{a}}$  positions, which corresponds to those with the more positive charges in  $\text{Ag}_{11}$  (Table 2). Those with the less positive charges in  $\text{Ag}_{11}$ , namely the  $\text{M}_{\text{tbp-eq}}$  positions, are the less favored positions. This site preference is maintained when doping with two and three Cu atoms, as shown in the middle and bottom of Fig. 7, which shows the positional isomers of lowest energy for the  $\text{Cu}_2\text{Ag}_9$  and  $\text{Cu}_3\text{Ag}_8$  compo-

sitions, respectively. A mixture of three isomers is expected in the case of  $\text{Cu}_2\text{Ag}_9$ , whereas only one is expected to be obtained (or at least as a largely dominant species) in the case of the trisubstituted  $\text{Cu}_3\text{Ag}_8$ .

## Conclusions

In summary, this investigation delves into the intricacies of metal addition and doping effects, utilizing a 2-electron  $\text{Ag}_{10}$  NC as a foundational template. The surficial traits of  $\text{Ag}_{10}$  uncover an open vacancy that facilitates the attachment of additional  $\text{Ag}^+/\text{Cu}^+$  ions, resulting in the formation of  $\text{Ag}_{11}$  and  $\text{Cu}_x\text{Ag}_{11-x}$ . Significantly, the solvent-dependent emission spectra shed light on the intricate interplay between the structural characteristics and the potent impact of solvent polarity, offering a window into the solvatochromic behaviors of these materials. Furthermore, the emission of these NCs extends into the near-infrared (NIR) region, which opens up potential applications in areas such as bioimaging and photothermal therapy. These insights underscore the robust nature of superatomic electronic properties, demonstrating their capacity for fine-tuning properties through controlled metal addition and doping, further expanding the functional versatility of metal NCs.

## Experimental section

## Materials and instrumentation

All chemicals used as received were purchased from commercial sources. Solvents were purified following standard protocols.<sup>51</sup> All reactions were performed in oven-dried Schlenk glassware using standard inert atmosphere techniques. All reactions were carried out under an N<sub>2</sub> atmosphere by using standard Schlenk techniques. Ag<sub>10</sub>(dtp)<sub>8</sub><sup>39</sup> and Au(PPh<sub>3</sub>)Cl<sup>52</sup> were prepared by procedures reported earlier in the literature. The <sup>1</sup>H and <sup>31</sup>P{<sup>1</sup>H} NMR spectra were recorded on a Bruker Avance II 400 MHz NMR spectrometer, operating at 400.13 MHz for <sup>1</sup>H, and 161.98 MHz for <sup>31</sup>P. The chemical shifts (δ) and coupling constants (J) are reported in ppm and Hz, respectively. The ESI mass spectrum was recorded on a QSTAR® XL (AB SCIEX, Warrington, Cheshire, U.K.).

X-ray photoelectron spectroscopy (XPS) spectra were recorded by using a PHI 5000 VersaProbe-Scanning ESCA Microprobe. UV-visible absorption spectra were recorded on an Agilent Cary 60 spectrophotometer using quartz cells with path length of 1 cm. The emission and QY spectra were recorded on a Horiba FluoroMax<sup>+</sup> fluorescence spectrometer equipped with a 150 W ozone free xenon lamp as the excited source, a detector with R13456P PMT, and NIR InGaAs. The lifetime was recorded on an Edinburgh FLS920 fluorescence spectrometer using the TCPSC technique, using an H<sub>2</sub> pulse lamp as the excited source and R928P as the detector. The QY was determined by a comparative method,<sup>53,54</sup> and the detailed results of the target complexes are shown in Table S3.† Absolute values are calculated by using [Ru(bpy)<sub>3</sub>]<sup>2+</sup> as the standard sample.<sup>55,56</sup>

## Synthesis

[Ag<sub>11</sub>(dtp)<sub>8</sub>(SO<sub>3</sub>CF<sub>3</sub>)], Ag<sub>11</sub>. [Ag<sub>10</sub>(dtp)<sub>8</sub>] (0.041 g, 0.0147 mmol) was dissolved in THF (30 mL). Ag(OTf) (0.0038 g, 0.0147 mmol) was added to this mixture and stirred continuously for 1 minute. It was dried under vacuum and the powder was washed with hexane. The precipitate was dried to yield purple powder as [Ag<sub>11</sub>(dtp)<sub>8</sub>(SO<sub>3</sub>CF<sub>3</sub>)]. Yield: 0.0436 g (97.5%, based on Ag). <sup>31</sup>P{<sup>1</sup>H} NMR (161.98 MHz, CDCl<sub>3</sub>, δ, ppm): 103.2, 100.8. <sup>1</sup>H NMR (400.13 MHz, CDCl<sub>3</sub>, δ, ppm): 1.40 (m, <sup>3</sup>J<sub>HH</sub> = 4 Hz, 96H, CH<sub>3</sub>), 4.82 (br, 16H, CH). UV-vis spectra [λ in nm (ε in M<sup>-1</sup> cm<sup>-1</sup>): 391 (20 600), 527 (9900)].

[**Cu<sub>x</sub>Ag<sub>11-x</sub>(dtp)<sub>8</sub>**](SO<sub>3</sub>CF<sub>3</sub>), **Cu<sub>x</sub>Ag<sub>11-x</sub>**. [Ag<sub>10</sub>(dtp)<sub>8</sub>] (0.041 g, 0.0147 mmol) was dissolved in THF (30 mL). [Cu(CH<sub>3</sub>CN)<sub>4</sub>](OTf) (0.0055 g, 0.0147 mmol) was added to this mixture and stirred continuously for 1 minute. It was dried under vacuum and the powder was washed with hexane. The precipitate was dried to yield purple powder as **Cu<sub>x</sub>Ag<sub>11-x</sub>**. <sup>31</sup>P{<sup>1</sup>H} NMR (161.98 MHz, CDCl<sub>3</sub>, δ, ppm): 94–105. <sup>1</sup>H NMR (400.13 MHz, CDCl<sub>3</sub>, δ, ppm): 1.40 (m, <sup>3</sup>J<sub>HH</sub> = 7 Hz, 96H, CH<sub>3</sub>), 4.82 (br, 16H, CH). UV-vis spectra [λ in nm (ε in M<sup>-1</sup> cm<sup>-1</sup>): 392 (20 100), 506 (8800)].

## X-ray crystallography

Single crystals suitable for X-ray diffraction analysis of **Ag<sub>11</sub>** were obtained by the slow evaporation of CH<sub>2</sub>Cl<sub>2</sub> solution at ambient temperature. Single crystals were mounted on the tip of a glass fiber with Paratone oil. Data were collected on a Bruker APEX II CCD diffractometer using graphite monochromated Mo K $\alpha$  radiation ( $\lambda = 0.71073$  Å) at 100 K. Absorption corrections for the area detector were performed with SADABS,<sup>57</sup> and the integration of the raw data frame was performed with SAINT.<sup>58</sup> The structures were solved by direct methods and refined by least-squares against  $F^2$  using the SHELXL-2018/3 package,<sup>59</sup> incorporated in SHELXTL/PC V6.14.<sup>60</sup> All non-hydrogen atoms were refined anisotropically. CCDC no. 2287343† (**Ag<sub>11</sub>**) contains the supplementary crystallographic data in this article.

## Computational details

For the sake of reducing computational effort, all calculations were made on simplified models in which the  $\text{S}_2\text{P}(\text{O}^i\text{Pr})_2$  ligands were replaced by the smaller  $\text{S}_2\text{P}(\text{OMe})_2$  ones.

Geometry optimizations were performed by density functional theory (DFT) calculations with the Gaussian 16 package,<sup>61</sup> using the BP86 functional<sup>62</sup> together with Grimme's empirical DFT-D3(BJ) corrections<sup>63</sup> and the Def2-TZVP basis set from EMSL Basis Set Exchange Library.<sup>64</sup> All the optimized geometries were characterized as true minima by vibrational analysis. The NAO charges and Wiberg bond indices were computed with the NBO 6.0 program.<sup>65</sup> The UV-visible transitions were calculated by means of time-dependent DFT (TD-DFT) calculations, using the B3LYP<sup>66</sup> functional and the Def2-TZVP basis set. The UV-visible spectra were simulated from the computed TD-DFT transitions and their oscillator strengths by using the SWizard program,<sup>67</sup> with each transition being associated with a Gaussian function of half-height width equal to 2000 cm<sup>-1</sup>. The compositions of the molecular orbitals were calculated using the AOMix program.<sup>68</sup>

## Conflicts of interest

There are no conflicts to declare.

## Acknowledgements

This work was supported by the National Science and Technology Council of Taiwan (112-2123-M-259-001) and the GENCI Computing Resource (grant A0090807367). The authors gratefully acknowledge the Instrumentation Center of National Taiwan Normal University (NSTC 111-2731-M-003-001) for its support.

## References

- 1 A. V. Artem'ev and C. W. Liu, *Chem. Commun.*, 2023, **59**, 7182–7195.
- 2 Y. Li and R. Jin, *Nanoscale Horiz.*, 2023, **8**, 991–1013.
- 3 M. F. Matus and H. Häkkinen, *Nat. Rev. Mater.*, 2023, **8**, 372–389.
- 4 J. Wei, D. M. Carey, J.-F. Halet, S. Kahlal, J.-Y. Saillard and A. Muñoz-Castro, *Inorg. Chem.*, 2023, **62**, 3047–3055.
- 5 R. Antoine, M. Broyer and P. Dugourd, *Sci. Technol. Adv. Mater.*, 2023, **24**, 2222546.
- 6 I. Chakraborty and T. Pradeep, *Chem. Rev.*, 2017, **117**, 8208–8271.
- 7 T. Chen, H. Lin, Y. Cao, Q. Yao and J. Xie, *Adv. Mater.*, 2022, **34**, 2103918.
- 8 X. Kang and M. Zhu, *Chem. Soc. Rev.*, 2019, **48**, 2422–2457.
- 9 H. Li, X. Kang and M. Zhu, *ChemPhysChem*, 2022, **23**, e202200484.
- 10 K. S. Krishna, P. Tarakeshwar, V. Mujica and C. S. S. R. Kumar, *Small*, 2014, **10**, 907–911.
- 11 M. Zhu, C. M. Aikens, M. P. Hendrich, R. Gupta, H. Qian, G. C. Schatz and R. Jin, *J. Am. Chem. Soc.*, 2009, **131**, 2490–2492.
- 12 S. Biswas, S. Das and Y. Negishi, *Nanoscale Horiz.*, 2023, **8**, 1509–1522.
- 13 Y.-M. Li, J. Hu and M. Zhu, *Coord. Chem. Rev.*, 2023, **495**, 215364.
- 14 Y. Du, H. Sheng, D. Astruc and M. Zhu, *Chem. Rev.*, 2020, **120**, 526–622.
- 15 G. Yang, Z. Wang, F. Du, F. Jiang, X. Yuan and J. Y. Ying, *J. Am. Chem. Soc.*, 2023, **145**, 11879–11898.
- 16 Y. Su, T. Xue, Y. Liu, J. Qi, R. Jin and Z. Lin, *Nano Res.*, 2019, **12**, 1251–1265.
- 17 Y. Li, M. J. Cowan, M. Zhou, M. G. Taylor, H. Wang, Y. Song, G. Mpourmpakis and R. Jin, *ACS Nano*, 2020, **14**, 6599–6606.
- 18 M. S. Bootharaju, C. W. Lee, G. Deng, H. Kim, K. Lee, S. Lee, H. Chang, S. Lee, Y.-E. Sung, J. S. Yoo, N. Zheng and T. Hyeon, *Adv. Mater.*, 2023, **35**, 2207765.
- 19 Y.-J. Zhong, J.-H. Liao, T.-H. Chiu, F. Gam, S. Kahlal, J.-Y. Saillard and C. W. Liu, *J. Chem. Phys.*, 2021, **155**, 034304.
- 20 S. Lee, M. S. Bootharaju, G. Deng, S. Malola, H. Häkkinen, N. Zheng and T. Hyeon, *J. Am. Chem. Soc.*, 2021, **143**, 12100–12107.
- 21 R. P. B. Silalahi, K. K. Chakrahari, J.-H. Liao, S. Kahlal, Y.-C. Liu, M.-H. Chiang, J.-Y. Saillard and C. W. Liu, *Chem. – Asian J.*, 2018, **13**, 500–504.
- 22 G. Soldan, M. A. Aljuhani, M. S. Bootharaju, L. G. AbdulHalim, M. R. Parida, A.-H. Emwas, O. F. Mohammed and O. M. Bakr, *Angew. Chem., Int. Ed.*, 2016, **55**, 5749–5753.
- 23 X. Liu, E. Wang, M. Zhou, Y. Wan, Y. Zhang, H. Liu, Y. Zhao, J. Li, Y. Gao and Y. Zhu, *Angew. Chem., Int. Ed.*, 2022, **61**, e202207685.
- 24 Y. Niihori, W. Kurashige, M. Matsuzaki and Y. Negishi, *Nanoscale*, 2013, **5**, 508–512.
- 25 S. Yang, J. Chai, Y. Song, J. Fan, T. Chen, S. Wang, H. Yu, X. Li and M. Zhu, *J. Am. Chem. Soc.*, 2017, **139**, 5668–5671.
- 26 F. Fetzer, C. Schrenk, N. Pollard, A. Adeagbo, A. Z. Clayborne and A. Schnepf, *Chem. Commun.*, 2021, **57**, 3551–3554.
- 27 Y.-R. Lin, P. V. V. N. Kishore, J.-H. Liao, S. Kahlal, Y.-C. Liu, M.-H. Chiang, J.-Y. Saillard and C. W. Liu, *Nanoscale*, 2018, **10**, 6855–6860.
- 28 Q. Tang, Y. Lee, D.-Y. Li, W. Choi, C. W. Liu, D. Lee and D.-e. Jiang, *J. Am. Chem. Soc.*, 2017, **139**, 9728–9736.
- 29 W. Rong, H. Zou, W. Zang, S. Xi, S. Wei, B. Long, J. Hu, Y. Ji and L. Duan, *Angew. Chem., Int. Ed.*, 2021, **60**, 466–472.
- 30 B. Rao, T. Zhao, S. Yang, J. Chai, Y. Pan, S. Weng, H. Yu, X. Li and M. Zhu, *Dalton Trans.*, 2018, **47**, 475–480.
- 31 J. Chai, Y. Lv, S. Yang, Y. Song, X. Zan, Q. Li, H. Yu, M. Wu and M. Zhu, *J. Phys. Chem. C*, 2017, **121**, 21665–21669.
- 32 J. Zhou, S. Yang, Y. Tan, H. Cheng, J. Chai and M. Zhu, *Chem. – Asian J.*, 2021, **16**, 2973–2977.
- 33 W.-J. Yen, J.-H. Liao, T.-H. Chiu, Y.-S. Wen and C. W. Liu, *Inorg. Chem.*, 2022, **61**, 6695–6700.
- 34 L. Tang, Q. Han, B. Wang, Z. Yang, C. Song, G. Feng and S. Wang, *Phys. Chem. Chem. Phys.*, 2024, **26**, 62–66.

- 35 F. Gam, I. Chantrenne, S. Kahlal, T.-H. Chiu, J.-H. Liao, C. W. Liu and J.-Y. Saillard, *Nanoscale*, 2022, **14**, 196–203.
- 36 Z. Gan, N. Xia and Z. Wu, *Acc. Chem. Res.*, 2018, **51**, 2774–2783.
- 37 A. Baksi, E. K. Schneider, P. Weis, I. Chakraborty, O. Fuhr, S. Lebedkin, W. J. Parak and M. M. Kappes, *ACS Nano*, 2020, **14**, 15064–15070.
- 38 X. Zou, Y. Li, S. Jin, X. Kang, X. Wei, S. Wang, X. Meng and M. Zhu, *J. Phys. Chem. Lett.*, 2020, **11**, 2272–2276.
- 39 Y.-J. Zhong, J.-H. Liao, T.-H. Chiu, S. Kahlal, C.-J. Lin, J.-Y. Saillard and C. W. Liu, *Angew. Chem., Int. Ed.*, 2021, **60**, 12712–12716.
- 40 C. W. Liu, Y.-R. Lin and C.-S. Fang, *Inorg. Chem.*, 2013, **52**, 2070–2077.
- 41 R. S. Dhayal, Y.-R. Lin, J.-H. Liao, Y.-J. Chen, Y.-C. Liu, M.-H. Chiang, S. Kahlal, J.-Y. Saillard and C. W. Liu, *Chem. – Eur. J.*, 2016, **22**, 9943–9947.
- 42 S. Chen, W. Du, C. Qin, D. Liu, L. Tang, Y. Liu, S. Wang and M. Zhu, *Angew. Chem., Int. Ed.*, 2020, **59**, 7542–7547.
- 43 W. Du, S. Jin, L. Xiong, M. Chen, J. Zhang, X. Zou, Y. Pei, S. Wang and M. Zhu, *J. Am. Chem. Soc.*, 2016, **139**, 1618–1624.
- 44 S. Wang, S. Jin, S. Yang, S. Chen, Y. Song, J. Zhang and M. Zhu, *Sci. Adv.*, 2015, **1**, e1500441.
- 45 M. Zhu, C. M. Aikens, F. J. Hollander, G. C. Schartz and R. Jin, *J. Am. Chem. Soc.*, 2008, **130**, 5883–5885.
- 46 W.-T. Chang, S. Sharma, J.-H. Liao, S. Kahlal, Y.-C. Liu, M.-H. Chiang, J.-Y. Saillard and C. W. Liu, *Chem. – Eur. J.*, 2018, **24**, 14352–14357.
- 47 Y.-J. Zhong, J.-H. Liao, T.-H. Chiu, Y.-S. Wen and C. W. Liu, *Molecules*, 2021, **26**, 5391.
- 48 P. Reineck and B. C. Gibson, *Adv. Opt. Mater.*, 2017, **5**, 1600446.
- 49 Y.-J. Zhong, J.-H. Liao, T.-H. Chiu, Y.-Y. Wu, S. Kahlal, M. J. McGlinchy, J.-Y. Saillard and C. W. Liu, *Dalton Trans.*, 2021, **50**, 4727–4734.
- 50 C. Reichardt, *Chem. Rev.*, 1994, **94**, 2319–2358.
- 51 D. D. Perrin and W. L. F. Armarego, *Purification of laboratory chemicals*, 3rd ed., Pergamon Press, Oxford, 1988.
- 52 M. I. Bruce, B. K. Nicholson, O. B. Shawkataly, J. R. Shapley and T. Henly, *Inorg. Synth.*, 1989, **26**, 324–328.
- 53 J. N. Demas and G. A. Crosby, *J. Am. Chem. Soc.*, 1970, **92**, 7262–7270.
- 54 J. N. Demas and G. A. Crosby, *J. Am. Chem. Soc.*, 1971, **93**, 2841–2847.
- 55 M. J. Cook, A. P. Lewis, G. S. G. McAuliffe, V. Skarda, A. J. Thomson, J. L. Glasper and D. J. Robbins, *J. Chem. Soc., Perkin Trans. 2*, 1984, 1293–1301.
- 56 K. Suzuki, A. Kobayashi, S. Kaneko, K. Takehira, T. Yoshihara, H. Ishida, Y. Shiina, S. Oishi and S. Tobita, *Phys. Chem. Chem. Phys.*, 2009, **11**, 9850–9860.
- 57 *SADABS version 2014–11.0*, Bruker Area Detector Absorption Corrections, Bruker AXS, Inc., Madison, WI, 2014.
- 58 *SAINT V8.30A*, Software for the CCD Detector System, Bruker Analytical, Madison, WI, 2012.
- 59 G. M. Sheldrick, *Acta Crystallogr., Sect. A: Found. Crystallogr.*, 2008, **64**, 112.
- 60 *SHELXTL Version 6.14*, Bruker AXS, Inc., Madison, WI, 2003.
- 61 M. J. Frisch, G. W. Trucks, H. B. Schlegel, G. E. Scuseria, M. A. Robb, J. R. Cheeseman, G. Scalmani, V. Barone, G. A. Petersson, H. Nakatsuji, X. Li, M. Caricato, A. V. Marenich, J. Bloino, B. G. Janesko, R. Gomperts, B. Mennucci, H. P. Hratchian, J. V. Ortiz, A. F. Izmaylov, J. L. Sonnenberg, D. Williams-Young, F. Ding, F. Lipparini, F. Egidi, J. Goings, B. Peng, A. Petrone, T. Henderson, D. Ranasinghe, V. G. Zakrzewski, J. Gao, N. Rega, G. Zheng, W. Liang, M. Hada, M. Ehara, K. Toyota, R. Fukuda, J. Hasegawa, M. Ishida, T. Nakajima, Y. Honda, O. Kitao, H. Nakai, T. Vreven, K. Throssell, J. A. Montgomery, Jr., J. E. Peralta, F. Ogliaro, M. J. Bearpark, J. J. Heyd, E. N. Brothers, K. N. Kudin, V. N. Staroverov, T. A. Keith, R. Kobayashi, J. Normand, K. Raghavachari, A. P. Rendell, J. C. Burant, S. S. Iyengar, J. Tomasi, M. Cossi, J. M. Millam, M. Klene, C. Adamo, R. Cammi, J. W. Ochterski, R. L. Martin, K. Morokuma, O. Farkas, J. B. Foresman and D. J. Fox, *Gaussian 16, Revision B.01*, Gaussian, Inc., Wallingford CT, 2016.
- 62 (a) A. D. Becke, *Phys. Rev. A: At., Mol., Opt. Phys.*, 1988, **38**, 3098–3100; (b) J. P. Perdew, *Phys. Rev. B: Condens. Matter Phys.*, 1986, **33**, 8822–8824.
- 63 S. J. Gimme, *Comput. Chem.*, 2006, **27**, 1787–1799.
- 64 (a) A. Schaefer, H. Horn and R. Ahlrichs, *J. Chem. Phys.*, 1992, **97**, 2571–2577; (b) A. Schaefer, C. Huber and R. Ahlrichs, *J. Chem. Phys.*, 1994, **100**, 5829–5835.
- 65 (a) E. D. Glendening, C. R. Landis and F. Weinhold, *NBO 6.0: Natural bond orbital analysis program*, *J. Comput. Chem.*, 2013, **34**, 1429–1437; (b) E. D. Glendening, J. K. Badenhoop, A. E. Reed, J. E. Carpenter, J. A. Bohmann, C. M. Morales, C. R. Landis and F. Weinhold, *NBO 6.0*, Theoretical Chemistry Institute, University of Wisconsin, Madison, WI, 2013, <https://nbo6.chem.wisc.edu>.
- 66 (a) A. D. Becke, *J. Chem. Phys.*, 1993, **98**, 5648–5652; (b) C. Lee, W. Yang and R. G. Parr, *Phys. Rev. B: Condens. Matter Mater. Phys.*, 1988, **37**, 785–789; (c) P. J. Stephens, F. J. Devlin, C. F. Chabalowski and M. J. Frisch, *J. Phys. Chem.*, 1994, **98**, 11623–11627.
- 67 S. I. Gorelsky, *SWizard program*, revision 4.5, <https://www.sg-chem.net>.
- 68 S. I. Gorelsky, *AOMix program*, <https://www.sg-chem.net>.